Acta Geotechnica (2023) 18:2827–2845
https://doi.org/10.1007/s11440-022-01673-8

RESEARCH PAPER

A novel method to improve the soil erosion resistance with fungi

Xijin Zhang[1] · Xudong Fan[2] · Chen Wang[3] · Xiong Yu[4]

Received: 23 June 2021 / Accepted: 4 August 2022 / Published online: 8 November 2022

Abstract

This study evaluated an innovative method to improve soil erosion resistance by fungi. An edible filamentous fungus, *Pleurotus ostreatus*, was included in the study. The result showed that *Pleurotus ostreatus* is able to grow and completely cover the circular surface of 60.20 mm diameter in 15 days when inoculated on the top surface and in 20 days when inoculated 5 mm under the soil surface. The erosion resistance of fungi mediated soil samples was evaluated by a Simplified Scour Resistance Test (SSRT). The results showed that fungi-mediated sand samples demonstrated much higher erosion resistance compared with control sand sample, both in terms of increasing the critical flow velocity and reducing the slope of erosion rate versus flow velocity curve. The mechanism of improved erosion resistance was investigated. The microstructure measured by SEM test showed that the sand particles were entangled by fungal fibers. Chemical precipitations were observed on sand surface and attached to fungal hyphae, which were identified as calcite, calcium oxalate monohydrate and calcium oxalate dihydrate by FTIR spectra and XRD analysis. The fungi mycelium surface showed hydrophobic behaviors with an average measured contact angle of 116.42°. The hydrophobicity generated slip along the interface. Analyses with computational fluid dynamics (CFD) model indicated that the slip due to the hydrophobicity of fungi reduced the shear stress at the water-soil interface, which also improved the erosion resistance by fungi-mediated sand.

Keywords Biomediated soil improvements · Biomineral precipitation · Contact angle · Erosion · Filamentous fungus · Hydrophobicity

✉ Xiong Yu
xxy21@case.edu

Xijin Zhang
xxz677@case.edu

Xudong Fan
xxf121@case.edu

Chen Wang
cwang33@tongji.edu.cn

[1] Department of Civil and Environmental Engineering, Case Western Reserve University, 2104 Adelbert Road, Bingham 249C, Cleveland, OH 44106, USA

[2] Department of Civil and Environmental Engineering, Case Western Reserve University, 2104 Adelbert Road, Bingham 248, Cleveland, OH 44106, USA

[3] Department of Geotechnical Engineering, Tongji University, Shanghai 200092, China

[4] Department of Civil and Environmental Engineering, Case Western Reserve University, 2104 Adelbert Road, Bingham 237, Cleveland, OH 44106, USA

1 Introduction

Soil erosion near the underwater foundation of bridge is a common risk to bridge safety [24]. The water stream forms a vortex while flowing around the bridge piers [26], which accelerates the flow near the foundation and carries away soil resulting in the loss of foundation support [21, 37–39].Soil scour erosion has been recognized to play a detrimental role in the performance of bridges under natural hazards [36]. The erosion of sediments around the foundation of bridge is responsible for almost two thirds of the total number of bridge failures in the United States [11]. From the 1960s to the 1990s, over 600 bridges collapsed in the United States due to the scour erosion around bridge pier or abutment [31]. The average annual cost for repairing bridges subjected to the scour problem is estimated at \$30 ∼ \$50 million [19]. Therefore, improving the erosion resistance of soil is essential to ensure the safety of bridges.

Various approaches are applied to mitigate the risk due to bridge scour. The traditional methods to mitigate soil erosion can be grouped broadly under two distinctive categories, i.e., passive countermeasures and active countermeasures [33]. The passive countermeasures are fulfilled by providing additional barriers to improve the resistance against the horseshoe vortex. The riprap and geobag are typically used in this practice [1, 6]. Riprap can be further improved by partially grouting that improves its stability [18]. Examples of active countermeasures include the use of a collar to control scouring around piers by diverting the downflow of water [1]. Other methods to improve the scouring resistance include the use of sacrificial pile and slot in the pile. However, the conventional methods require significant construction labor and considerable monetary investment. Some of them also have a negative influence on the environment [3].

Microbial Induced Calcite Precipitation (MICP) was proposed as an emerging technique to prevent road shoulder erosion and bridge scour without human intervention [3]. MICP utilizes microorganisms to modify soil properties by facilitating calcium carbonate precipitation [7, 32]. Polymer-modified MICP treatment was demonstrated by Wang [35] to deal with the problem that the underlying soil was untreated by surficial MICP treatment. The hydrolysis by-product of MICP contains ammonium ions, which raised environmental concerns due to increasing ammonia emissions to the ecosystems [14, 17, 24]. It is desirable to develop sustainable techniques with less impact on the environment.

Therefore, another common microorganism, filamentous fungus, was chosen in this study to improve the soil erosion resistance. The fungal fibers have been reported with high strength and it can be grown with environmentally friendly feeding substrate. Filamentous fungi are a large fraction of total microbial biomass on the surface of earth. Fungi are known to produce oxalic acid, which reacts with metal ions. The calcium-oxalate associated with fungal hyphae are commonly observed in the sample both in the natural environment and in the experimental laboratory [37–39]. Fungi can also act as a natural fiber network to reinforce the surrounding soils and provide sites for calcium precipitation attachments [4, 16]. The common nutrition medium used for fungal growth, of which most ingredients are derived from potato, is environmentally friendly. Fungi also secrete small proteins called hydrophobins, which have been attributed to a wide spectrum of functions in fungal growth and interaction with soils [30]. For example, fungi influence the hydrophobicity of soil, contributing to the reduction of water infiltration and the increases in the stability of soil aggregates [27]. Recent studies indicated that a velocity slip occurs over hydrophobic surfaces, reducing the drag force at the interface correspondingly. When a surface is treated with a hydrophobic coating, a noticeable drag reduction in the flow is observed [13].

In this study, the fungus, *Pleurotus ostreatus*, was inoculated on the top surface and in the middle layer of sand samples to improve their scouring resistance. The growth behavior of fungal mycelium is observed at different incubation periods. Then, the scour resistance test is carried out to evaluate the anti-scouring performance of fungi mediated soil, of which results were compared to that of the control soil sample. The microstructure of the fungi-mediated soil sample is examined to investigate the mechanism for the improved the soil scouring resistance by fungal mycelium. The surface property of fungal mycelium was studied by measuring contact angle. Its impact on shear force generated by flowing water was investigated by a computational fluid dynamics (CFD) model.

2 Experimental materials

2.1 Sand

A standard ASTM sand was used in this study. The soil samples were oven-dried for 24 h. It has a specific gravity of 2.68 at 20° C. The laboratory tests categorized the sand as poorly graded sand with uniformity coefficient of 2.92 and coefficient of gradation of 1.31. The median grain size, D_{50}, was evaluated as 0.55 mm. The grain size distribution curve of soil particles is shown in Fig. 1. The sand sample has a density of 1.5 g/cm^3. The measured internal friction angle and cohesion are 30° and 0 kPa, respectively.

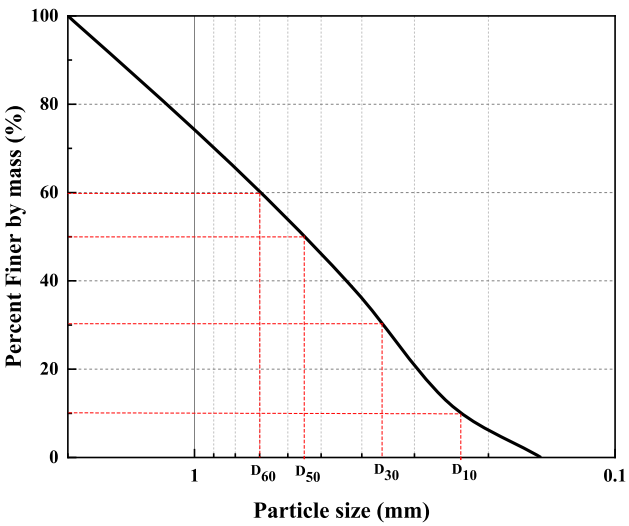

Fig. 1 Grain size distribution curve of sand sample

2.2 Fungal strain and culture medium

The edible filamentous fungus, *Pleurotus ostreatus* (*P. ostreatus*), was utilized in the study. This fungi strain has been found to produce fibers that have superior mechanical properties with a fast growth rate. *P. ostreatus* was purchased from the Mushroom Spawn Laboratory (Pennsylvania State University). It has been certified as not a biohazard [37–39]. BD Difco™ Dehydrated Culture Media Potato Dextrose Broth (PDB) and calcium chloride, produced by Fisher Scientific, were used to cultivate fungal strains. The culture medium was obtained by dissolving PDB and calcium chloride powder into deionized water with concentrations of 24 and 20 g/L respectively and stirring until the solution is homogeneous.

The autoclaving technique was applied to sterilize samples and tools. Both the culture solution and sand samples as well as the containers (250 mL beakers) were autoclaved at 120 °C for 15 min prior to use for inoculating fungi.

3 Experimental design

Comparative tests were conducted to investigate the effects of contributing factors on fungal behaviors to determine the best experimental conditions. The sand particle size and inoculated depth of fungi are considered. The fungal growth behaviors, including the germination of spores and the development of fungal mycelium, were utilized to evaluate the performance of different fungal placement.

3.1 Effects of sand particle size

We investigated the effects of particle size on fungal growth. Fine sand and coarse sand are used to study the effects of particle size on the development of fungal mycelium. The fine sand is 30–100 Nevada sand with a specific gravity of 2.68, and a relative density of 1.5 g/cm^3 at 20 °C. The parameters of coarse sand are the same as the description in Sect. 2.1.

Fungal mycelium germinated through the spread of fungal spores from different locations that are far away from the original fungal inoculum on the surface of fine sand. Fungal mycelium developed from the edges of the original fungal inoculum on the surface of coarse sand. The surface area of fungal mycelium in the coarse sand sample is much larger than that in the fine sand sample. Twenty days later, the fungal mycelium covered the surface of coarse sand with a diameter of 64.20 mm. However, the mycelium grew and only partially covered the surface of fine sand. Compared to the mycelium on fine sand surface, fungal mycelium is much thicker while growing on the surface of coarse sand after an incubation period of 20 days. These observations indicate fungi grow better in coarse sand than fine sand.

The mechanism behind this phenomenon is attributed to the favorable growing environment in coarse sand sample. The origin of the fungal growth was the germination, of which three phases are autoactivation, spore swelling and amoebal emergence. Spores were produced by filamentous fungi and were characterized by a dormant state initially [9]. Fungal spores are adapted for nutrition detection over a distance of a few centimeters [22]. Quick uptake of water, nutrients, and oxygen resulted in a shorter germination time [9]. The larger pore size in the coarse sand sample is favorable for the swelling and germination of spores, which also facilitates the mobilization of spores on the sand surface. The main component of fine sand is SiO_2. Various chemical components are in the coarse sand sample. For example, the germination of spores is dependent on the activity of calcium. Calcium is an essential cation for the regulation of protein calmodulin during the germination of fungal spores [20]. Calcium also has a regulatory impact on the formation of spores as well as hyphal growth [10]. The substrate enriched with calcium promotes the mycelium development and bonding performance [2]. Therefore, the coarse sand provides a beneficial neighboring environment for the germination of spores and the development of fungal mycelium.

3.2 The effects of fungi inoculation depth

Inoculated depth is defined as the thickness of sand cover above the location fungal inoculum was placed. Four inoculated depths (5, 10, 15, and 20 mm) are used to investigate its impact on fungal growth. Only the fungal inoculum at the first layer (inoculated depth 5 mm) germinated, which was evidenced from the front view of each sample. After 20 days, we removed the fungal mycelium from each sample and left the sand without fungal mycelium. We also measured that the average depth in the fine sand and coarse sand samples are about 6.3 and 5.5 mm, respectively. This indicates that the fungal inoculum develops from the inoculated depth of 5 mm. They preferred to grow on the upper layer for a greater supply of oxygen and developed to 0.5–1.3 mm beneath the inoculated depth layer.

Larger embedment depth of fungal inoculation is desirable since this facilitates the reinforcement of fungal mycelium on sand samples. However, the increased embedment depth inhibits the fungal growth due to the reduced oxygen supply and introducing overlain pressure that might suppress spore germination. From the four inoculation depths analyzed in this study, the inoculation

depth of 5 mm achieved the best performance, which produced reinforcement effects on the upper layer of sand sample and as well as 0.5 to 1.3 mm beneath the inoculated layer.

From these observations, coarse sand and inoculated depth of 5 mm were utilized in this study to ensure the fungal growth in the sample. Calcium ions were added in the nutrition to facilitate the germination of fungal spores as well as the precipitation rate in sand samples.

3.3 Contrast groups of final experimental samples

Three groups of samples were prepared, including one group with fungi inoculated on the top surface of soil sample (FS-T), one group with fungi inoculated inside the soil sample (FS-M), and one group of pure sand sample as the control group (S). Samples were prepared with glass beaker with an inner diameter of 64.20 mm and a height of 90 mm. Energy control was used to produce consistent initial soil density condition in different samples, the dry sand fell through a funnel with a constant height of 150 mm above surface. Sand was deposited layer by layer until reaching the height of 30 mm. All the procedures in the control group (S) are the same as in the test group (FS-T and FS-M) except the inoculation of the fungal disc. Disc with a diameter of 5.75 mm was cut from the leading edge of the original fungal colony using a glass cork borer after being flame sterilized. The fungal disc of *P. ostreatus* was inoculated at the center of the soil surface at heights of 30 mm (FS-T) and 25 mm (FS-M) for germination of the mycelia. An additional layer of sand with 5 mm thickness is deposited to cover the inoculum of *P. ostreatus* in FS-M. 30 mL culture solution was added to the surface of soil sample when inoculum is placed. The containers were covered with plastic wrap with air ventilation holes to allow oxygen supply to the fungi, while limiting the evaporation of culture medium to the extent possible. The temperature was controlled to be 20 ± 2° C and the relative humidity was 35 ± 3% during the incubation period of fungi mycelium.

The samples were saturated by supplying water into the sample container using a small tube carefully. The sample was saturated for 24 h prior to conducting the scour resistance test.

4 Experimental characterizations

4.1 SEM and EDS analyses on the microstructure of fungi

The SEM and EDS tests were conducted to observe the microstructure and morphological features of fungi-mediated soil samples with the Helios NanoLab 650. The samples were pre-dried in the oven at 50 °C for 24 h. Samples were coated by Pd with 4 nm for 30 s. It applied a voltage of 5 kV in a high vacuum mode when conducting

Table 1 The observed effects of sand particle size on fungal growth behaviors

	0 d	7d	20 d	Front view (20 d)
Fine sand				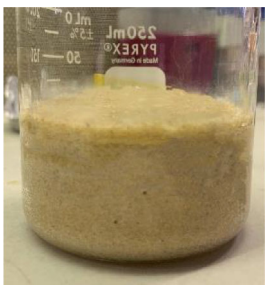
Coarse sand				

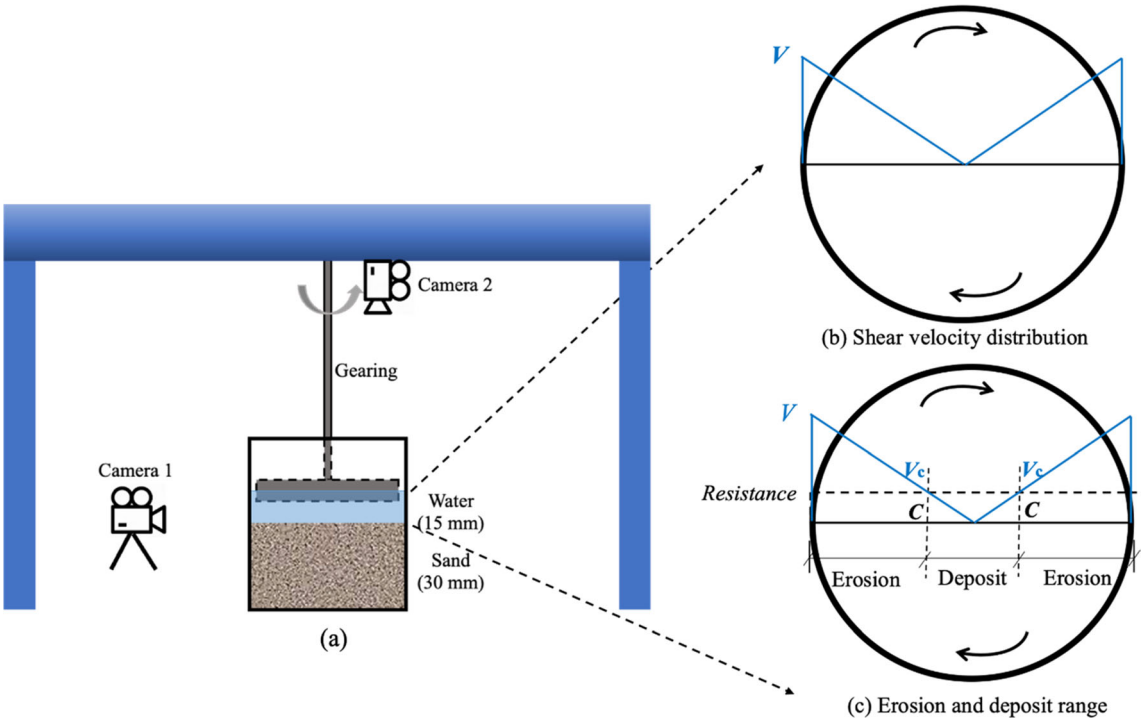

Fig. 2 (**a**) Anti-scouring experimental setup; (**b**) shear velocity distribution; (**c**) erosion and deposit area on soil surface

SEM tests on samples. The images were collected with a working distance of 4 mm. A current of 16 nÅ and a voltage of 15 kV were applied for the EDS analyses.

4.2 The Fourier-transform infrared (FTIR) spectra for the interaction between fungi and sand

The fungal mycelium grown in soil sample (FS-M) and control soil sample (S) was obtained to measure the Fourier Transform Infrared (FTIR) spectra with an Agilent Technologies Cary 630 FTIR spectrometer. The infrared spectra were set for the range from 400 to 4000 cm^{-1}. It provides information on chemical constituents of the fungal hyphae grown in sand.

4.3 X-ray diffraction for the precipitation identification

The Bruker D8 r-ray diffractometer with 1D with Cu sources and 2D detector with Co sources was used for characterizing the crystalline structure of precipitation produced by the interaction between fungi and sand particles. X-ray diffraction (XRD) is a nondestructive technique that allows investigating structures, phases, and crystal orientations of precipitation produced by fungal hyphae around sand particles. The samples were dried in the oven at 50 °C for 24 h and ground to fine powders by a pestle prior to the analysis. The filtered powder samples are scanned from 10–90 degrees with a resolution of 0.04 degrees per second.

4.4 Contact Angle for the surface property of fungal mycelium

The surface property of fungal mycelium was evaluated by the measured contact angle with a goniometer (KSV CAM200 Instruments Ltd). The contact angle is influenced by the surface free energy and is associated with surface tension of mycelium surface. Mycelium film was obtained from the sample (FS-T) and the specified volume of distilled water was dispersed from the syringe pump onto the fungal mycelium film. This process was controlled by the system with a constant dispersing speed and the contact angle of water on fungal mycelium was captured by a high-resolution camera. Five different locations on fungal mycelium were chosen randomly for the contact angle measurements. The left and right contact angles at the water-mycelium interface were analyzed by the image analysis software and subsequently averaged. The above procedures were repeated for five times on each of five mycelium samples. All readings were then averaged to give an averaged contact angle. The temperature was controlled to be 23° C and the relative humidity was 30 ± 2%. (Table 1).

Table 2 The observed effects of inoculated depth on fungal growth behaviors

	0 d	7d	20 d
Fine sand			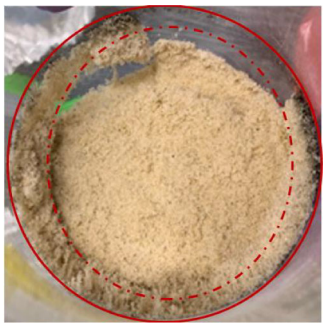
Coarse sand			

Table 3 Summary of taken images in each group

Specimen No	Top view				Front view
	0 d	5 d	15 d	20 d	20 d
S					
FS-T					
FS-M					

4.5 Anti-scouring experiment

The Simplified Scour Resistance Test (SSRT) setup shown in Fig. 2 as designed by [34] was used to measure the scour resistance. It includes a blade with a width of 64 mm and a height of 15 mm. The rotation of the blade was controlled at a preset speed to simulate the moving fluid flow. Under steady state conditions, the flow speed will linearly increase along the radius direction. The rotating speed of the blade could be set to range from 0 to 300 rounds per minute to simulate various local flow speeds in the range of 0–1.0 m/s. The testing samples were placed under the SSRT. The water level is controlled to be 15 mm above the soil–water interface. Two cameras were placed on the sides and on the top of the sample to record the dynamic behaviors at the soil–water interface and mycelium-water interface. (Table 2).

5 Results and discussions

5.1 Visual observation of fungal growth

Images were taken to record the development of fungal mycelium in soil samples and on the soil surface. Fungal growth, including fungal germination and their mycelial development, were observed in the two groups with the inoculum of *P. ostreatus* on the top and middle of the sand (FS-T and FS-M). A representative set of images are summarized in Table 3.

Fungi germinated rapidly and grew vigorously in the group of FS-T, where fungi were inoculated at the top and provides a favorable environment for fungal growth. It took 15 days for the growing mycelium to completely cover the sand surface in the FS-T group. The images in the FS-M group showed that fungal mycelium grew only slightly into the soil through the pore space. Compared to the FS-T group, the growth in the FS-M group was delayed, possibly due to the addition of soil layer that reduces the oxygen supply and introduces overlaying pressure. It took 20 days of growth for the fungal mycelium to completely cover the sand surface in the FS-M group (shown in Table 3). From the front view of sample FS-M, fungal hyphae developed through the void spacing between sand particles and exposed to the surface of sand. The fungal fiber interacts with sand and produced a physical reinforcing effect on the top layer of soil sample.

5.2 Erosion behaviors

The scour resistance tests were conducted on the three groups of soil samples and their dynamic behaviors were

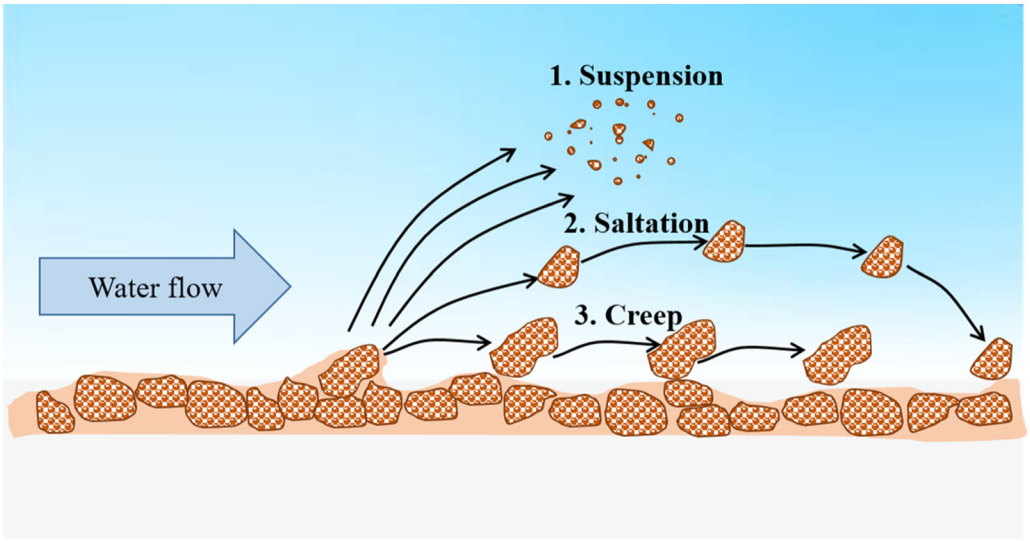

Fig. 3 Illustration of three movements of soil particles under water flow (Modified from [25])

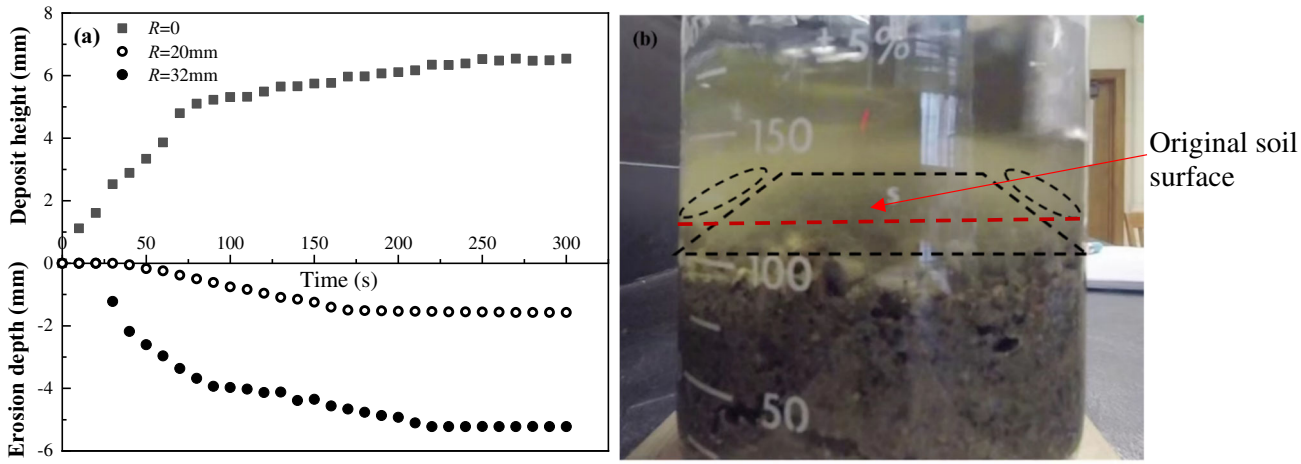

Fig. 4 Scouring behavior of control soil sample (S) at 120 rpm. (**a**) development of erosion depth and deposit height at different radius locations; (**b**) illustration of the deposit area and erosion area

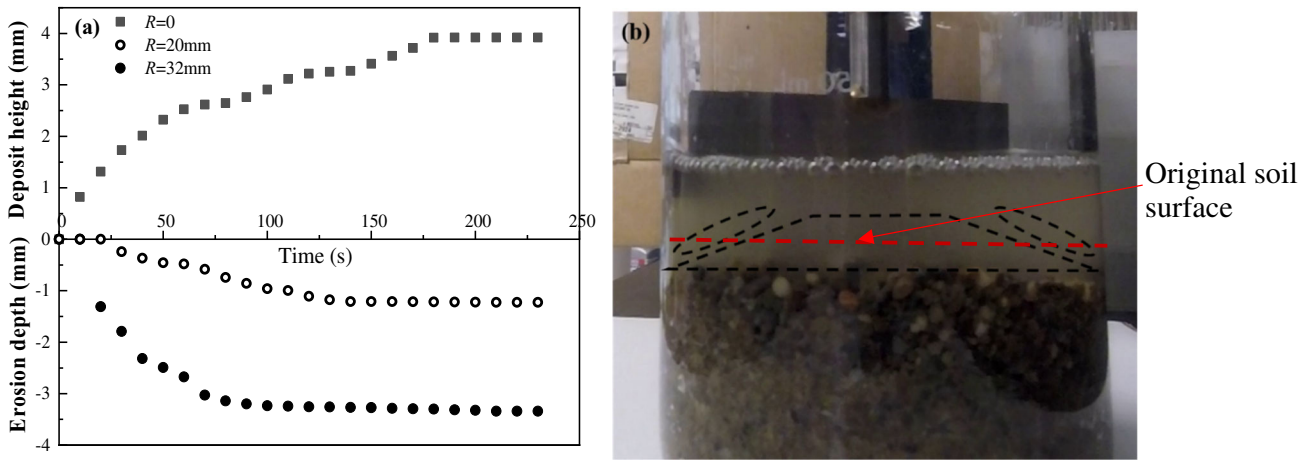

Fig. 5 Scouring behavior of fungi mediated soil sample (FS-T) at 300 rpm. **a** the development of erosion depth and deposit height at different radius locations; **b** illustrate of the deposit area and erosion area

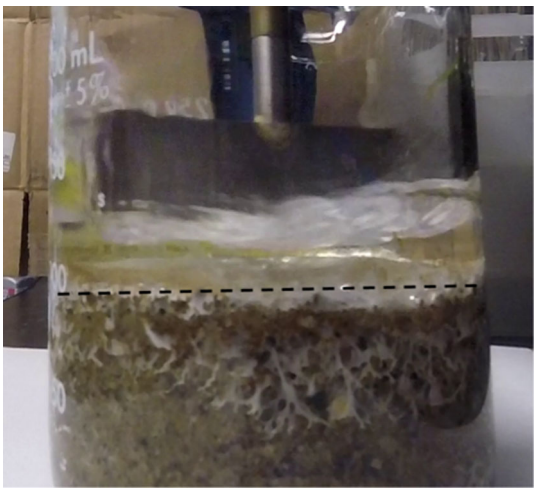

Fig. 6 Scouring behavior of fungi mediated soil sample (FS-M) at 300 rpm

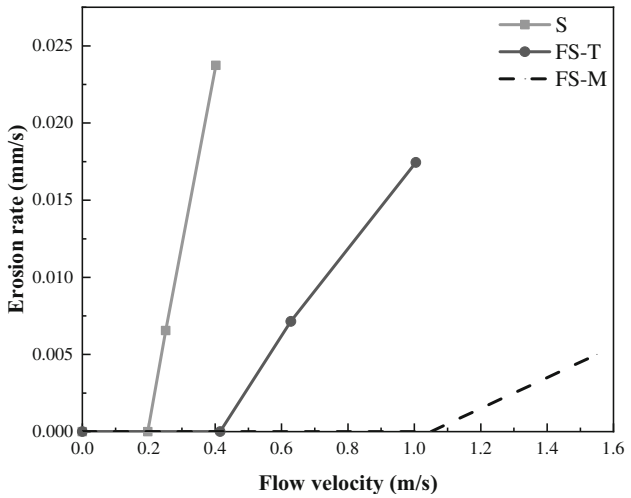

Fig. 7 Erosion curve of soil samples (S: control soil sample, FS-T: fungi mediated soil sample with fungi inoculated on the top of soil, FS-M: fungi mediated soil sample with fungi inoculated in the middle of soil

recorded by the cameras. In each group, the initial rotation speed was controlled at 120 rounds per min. The soil erosion behaviors are depended on the flow rate that varies at with the radius from center. The movement of soil particles were initiated when the flow velocity exceeded the critical value (u_c). With the increasing liner flow velocity away from the center, the erosion was observed at the edge of the soil sample firstly. Three types of movement occurred in along the surface of the soil sample as illustrated in Fig. 3, which were dependent on the particle size, flow velocity, as well as surface characteristics. The small particles suspended in water flow increased the turbidity of water; medium particles bounced or jumped after gaining energy from water flow; larger particles were too massive to be lifted and rolled along the surface until stopped by other particles. With the increasing blade rotation speed, the zone of soil erosion developed from the edge to the center until achieving an equilibrium state at a certain radius.

The scouring behavior at a few locations (R = 0, 20, and 32 mm) of the control soil sample (S) at 120 rpm is shown in Fig. 4a, based on analyzing the recorded video. It took 280 s to reach a stable status under rotating flow at 120 rpm. Soil erosion zone and deposition zone were observed. Soil particle erosion occurs at larger diameter, while deposition occurred at smaller diameter. At the equilibrium state, the erosion depths at R = 20 mm and 32 mm were 1.84 and 5.22 mm and the deposit height at the center was 6.54 mm. The radius of deposit area of sample S was 16.30 mm.

No obvious soil erosion was observed in sample with fungi inoculated at top surface (FS-T) at 120 rpm. The mycelium was separated from the edges of the soil surface and quickly floated on the water surface after increase the rotating speed to 170 rpm within 3 s. After removing the floating mycelium, no erosion was observed on the soil sample at 170 rpm. When further increasing the rotational speed to 300 rpm, the observed scouring behavior at different radius (R = 0, 20, and 32 mm) of sample FS-T is shown in Fig. 5. The equilibrium state reached after 190 s and the erosion depths at R = 20 mm and 32 mm were 1.23 and 3.34 mm; the deposit height at the center was 3.92 mm. After the scour resistance test, the morphology of the water-soil interface was observed. The radius of the deposit area in FS-T sample at 300 rpm was 13.22 mm. The water has less turbidity in the FS-T sample event at 300 rpm compared to that of control soil sample at 120 rpm.

Various rotating flow speeds (120, 170, and 300 rpm) were also applied on the sample with fungi inoculated at 5 mm under surface (FS-M). The soil surface in FS-M was not eroded by the rotating flow at 120 and 170 rpm. Even when the rotation speed of the blade was increased to 300 rpm, soil sample with fungal mycelium remained intact (Fig. 6). Fungal mycelium improved soil erosion resistance and works as a shield against water erosion. Water does not develop turbidity when the sample FS-M was subjected to the scouring test.

Soil erosion curve is commonly plotted by the erosion rate versus flow velocity. In this study, the average erosion rate was defined as the 99% equilibrium erosion depth divided by the corresponding time; the flow velocity along the radius was calculated by Eq. (1).

$$u = n\pi R/30 \quad (1)$$

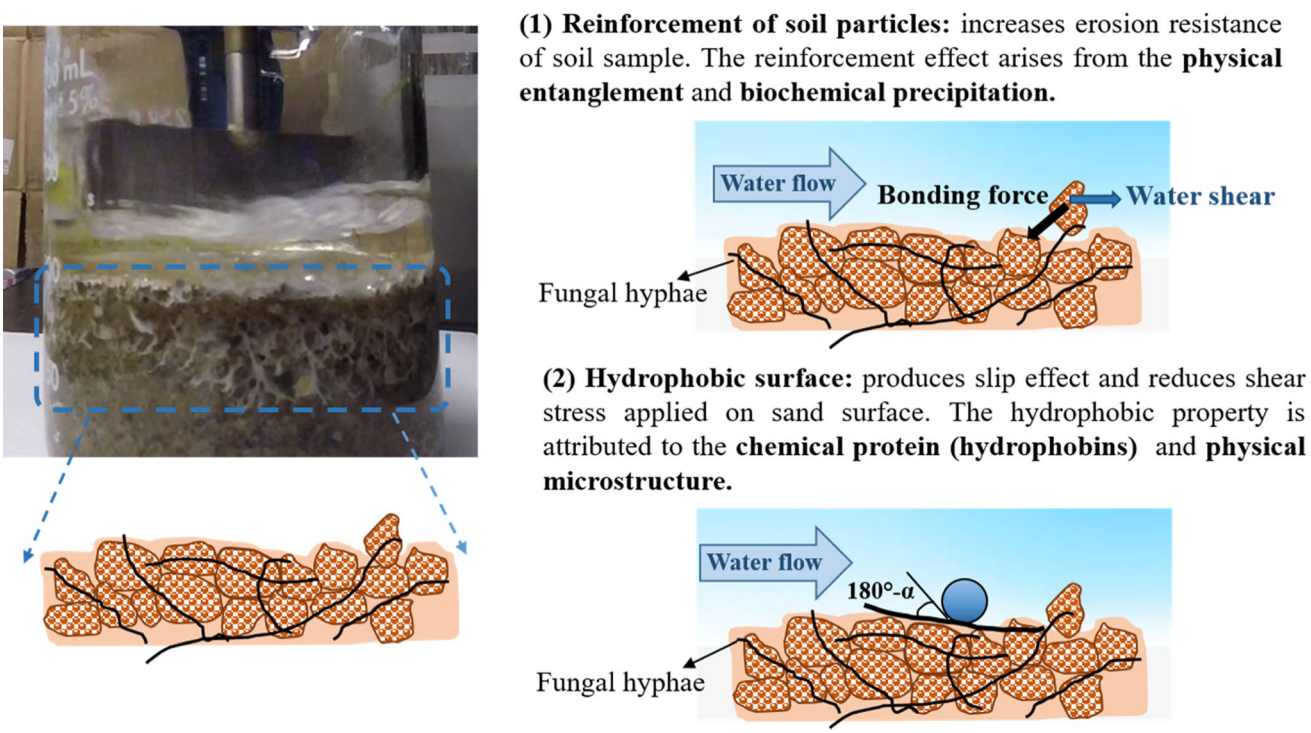

Fig. 8 Scheme of scouring resistance improvement by fungal mycelium

where u is the shear velocity, n is the rotating speed in rpm, and R is the located radius. The critical shear velocity is the velocity (u_c) at the critical point (C) of deposit range.

The critical shear velocity, u_c, which is the flow velocity above which erosion initializes (or the x-intercept of the soil erosion curve), is evaluated as the velocity at the boundary of erosion and deposit zone. When the water velocity exceeds the critical velocity, soil will experience erosion. From the experimental data, the critical shear velocity occurred at the critical point at radiuses of 16.30 and 13.22 mm respectively in the sample S and FS-T. These corresponded to critical flow velocity of 0.2 and 0.4 m/s, respectively. The critical velocity of FS-M was estimated to be larger than 1.0 m/s. The corresponding average erosion rate were calculated and plotted versus flow velocity of sample S and FS-M in Fig. 7. The erosion curve of control soil sample S was plotted as a baseline.

Compared with the control soil sample, fungi mediated soil samples show much larger critical flow velocity and much smaller slope of the erosion curve, both indicating improved soil erosion resistance. That is, under the same flow speed, fungi mediated soils featured much smaller erosion rate. The improved soil erosion resistance by fungi was attributed to the reinforcement of soil particles interactions by the fungal hyphae fiber.

5.3 The mechanism of improvement of scouring resistance by fungal mycelium

The observed scouring behaviors indicate fungi mycelium enhanced the erosion resistance of soil samples. Fungal mycelium was able to grow through the soil pores and on the soil surface. These improved the anti-scouring properties of soil samples. The mechanisms include (1) The reinforcement of soil particles by fungi hyphae fiber and (2) The hydrophobic behaviors of fungal mycelium that changes the soil–water surface interactions, which are illustrated in Fig. 8. The fungi fiber reinforcement enhanced the soil erosion resistance by increasing the critical velocity as well as the slope of soil erosion curve. The hydrophobicity of fungi fiber reduced the shear stress applied on the soil–water interface, which lead to higher critical shear velocity.

5.3.1 Reinforcement by fungal hyphae

5.3.1.1 Microstructure of fungi reinforced soil To observe the interactions between sand particles and fungal mycelium in the microscale, scanning electron microscopy (SEM) images were collected. Figure 9a presents the surface texture of plain sand. Figure 9b shows that amorphous residue of nutrients was found in the control sand (sample S). Figure 9c and d shows the SEM images of FS-M samples. As can be seen from this sample, the sand surface

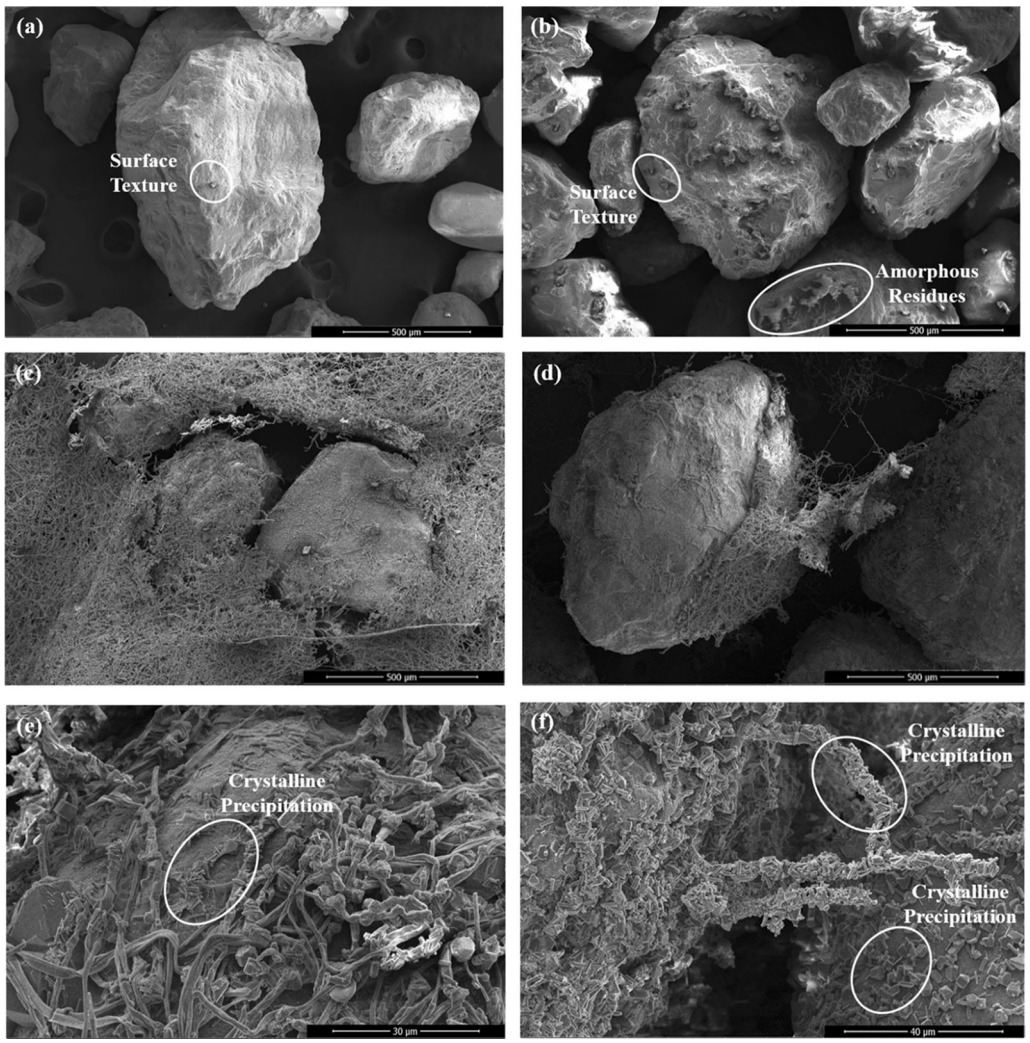

Fig. 9 Microstructure of fungi-mediated soil sample. **a** Untreated sand particles. **b** Sand particles from sample S. **c** Sand particles covered by fungal mycelium. **d** Sand particles entangled by fungal hyphae. **e** Fungal hyphae and precipitation on sand surface. **f** Sand particles bonded by precipitation and fungal fibers

was covered by fungal mycelium and the sand particles were reinforced by numerous fungal hyphae. Moreover, abundant fungal fibers were observed to grow on the surface of sand particles. Along with fungal hyphae, a large amount of crystalline precipitation was attached to the surface of fungal hyphae as well as the sand particles. Two types of crystals, one of which is cube and the other is needle, were found on the surface of fibers and sand. Figure 9f reveals two sand particles bridged by several fungal fibers, with many mineral precipitations attached along the fibers. The mineral precipitations mediated by fungi contributed to the bonding and reinforcement among sand particles. These facilitate the improvement of the erosion resistance of the soil samples.

Elements mapping by energy-dispersive x-ray spectroscopy (EDS) in the scanning electron microscopy (SEM) was applied for the analysis of chemical composition in the selected areas containing the two types of mineral precipitations. Figure 10a shows the cube precipitation attached on fungi hyphae. The weight percentage (Wt.%) and atomic percentage (At.%) of each element were shown in Table 4 (Carbon was not included since carbon tape was used for stabilizing samples on the holder). The precipitation crystals mainly composed of Oxygen (with Wt.% of 42.17 and At.% of 63.49), Calcium (with Wt.% of 36.66 and A.% of 22.03), and Chlorine (with Wt.% of 19.83 and At.% of 13.48). The existence of Carbon, Calcium, and Oxygen are evidenced in Fig. 10a (cube attached to fibers), arising from the precipitation produced by fungi. Secondly, Chlorine can be excluded from the composition of crystal (dark region shown in Fig. 10e). Another area was selected to represent the crystal with needle shape (Fig. 11a). The analysis of weight ratio and atomic ratio show the similar conclusion to that of cube crystals. The elemental

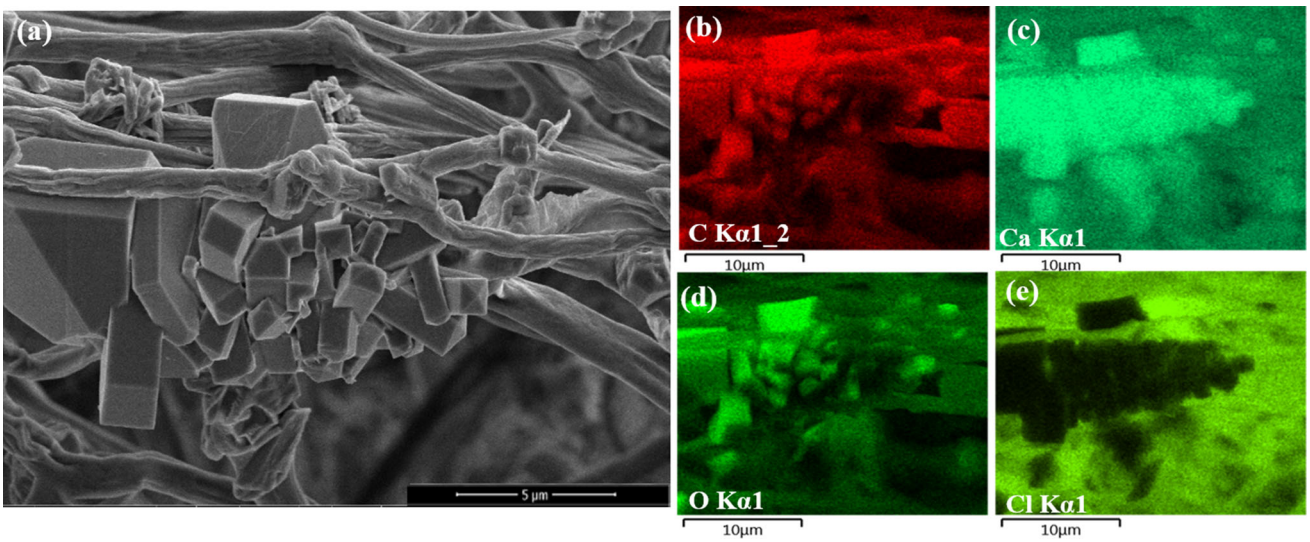

Fig. 10 EDS analysis of fungal hyphae attached by precipitation **a** Selected area 1 of hyphae along with produced precipitation. Selected area 1 EDS elemental mapping images of **b** C, **c** Ca, **d** O, and **e** Cl

mappings also indicated the existence of Carbon, Calcium, and Oxygen and excluded the existence of Chlorine in the precipitation. Additionally, the size of cube crystal is much larger than that of needle crystal. The averaged edges of cube crystal are about 7–10 µm, and the length of needle crystal is about 4–5 µm and width is 2 µm. The identification of the mineral precipitation is further analyzed with XRD and will be discussed in Sect. 3.3.1.3.

5.3.1.2 Chemical interactions between fungi and soil In order to clarify the chemical interaction between fungi and soil, Fourier Transform Infrared (FTIR) spectra of samples were obtained from control soil (S) and fungi mediated soil (FS-M). The main peaks and bands in sample S were characterized by a broad band between 827 and 1244 cm^{-1} and sharp bands at 511, 694, 777, and 796 cm^{-1}, which were corresponding to quartz (Institute of Chemistry University of Tartu) shown in the upper pattern in Fig. 12. FTIR spectra of sample FS-M shows the same peaks with sample S, including sharp bands at 694, and 1163 cm^{-1}. The peaks at 775, and 788 cm^{-1} in spectra of sample FS-M were attributed to the combined peaks of 777 and 796 cm^{-1} (from quartz) with peak of 725 cm^{-1} (symmetric CO3 band) [28]. The peak at 997 cm^{-1} reveals a combined area contained several bands appearance, including that, appears at 1057 cm^{-1} (from quartz), at 874 and at 1090 cm^{-1} (vibration of the carbonate ions) [28]. The broad band between 1401 and 1459 cm^{-1} were corresponding to the main asymmetric CO_3 band and vibration of the carbonate ions [28]. The peak at 1316 cm^{-1} was attributed to the vibration of the oxalate group), and the broad band between 1619 and 1643 cm^{-1} as well as the peak at 955 cm^{-1} were corresponding to the existence of calcium oxalate [37–39]. The peak at 517 cm^{-1} is due to the chemical bond Ca-O in calcium oxalate [28]. The broad band between 3000 and 3500 cm^{-1} was corresponding to the fungal indigents [37–39]. It indicates that there exist calcium carbonate and calcium oxalate in the sample FS-M.

5.3.1.3 Identification of Mineral Precipitation To identify the phase of precipitation produced by fungi, 1D XRD was utilized to investigate the powder materials gained from sample S and sample FS-M. There are three polymorphs, i.e., calcite (C), aragonite (A) and vaterite (V), included in Calcium carbonate ($CaCO_3$) [8]. Calcium oxalate (CaC_2O_4) contains in nature two polymorphs, i.e., whewellite (calcium oxalate monohydrate, COM) and weddellite (calcium oxalate dihydrate, COD) [40]. The 1D XRD patterns of sample S shows a mixture of various mineral crystals are contained in sand (S). The results of sample S also confirmed the existence of quartz and the absence of calcite, whewellite, and weddellite. The residue of nutrients on the surface of Sample S are amorphous and will therefore have limited influence on the bonding strength between sand particles. Therefore, the impact of residues on the improvement of erosion resistance in sample S is negligible.

Results of XRD in Fig. 13 indicates the existence of calcite and quartz as well as multiple crystals in fungi mediated soil sample (FS-M). 2D XRD with Co sources was applied on the powder materials of fungal mycelium separated from sample FS-T. (Fig. 14). The crystals of fungal mycelium in FS-T sample are identified as a mixture of calcite, whewellite, and weddellite [15]. The main peaks at 2θ = 23.03, 35.94, 43.12, and 69.11 ° belonged to the

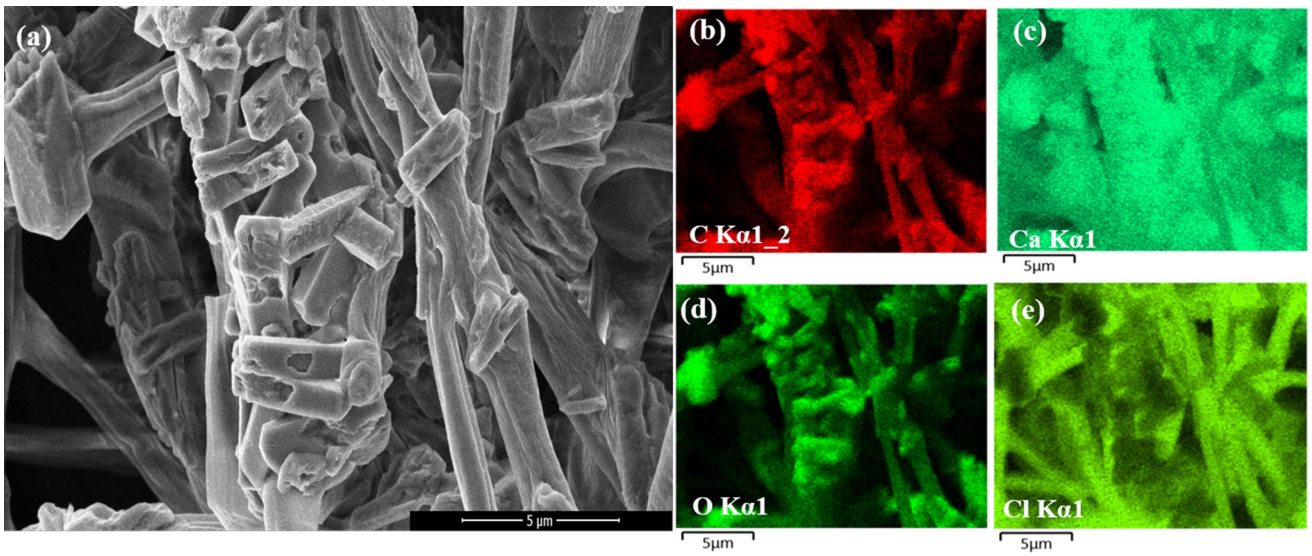

Fig. 11 EDS analysis of fungal hyphae attached by precipitation **a** Selected area 2 of hyphae along with produced precipitation. Selected area 2 EDS elemental mapping images of **b** C, **c** Ca, **d** O, and **e** Cl

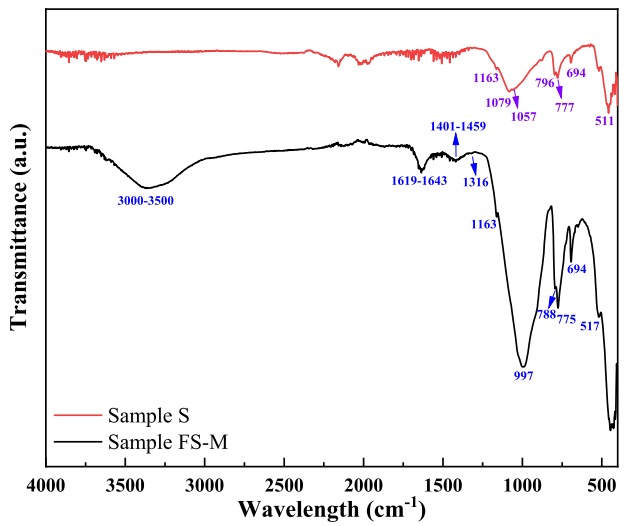

Fig. 12 FTIR spectra of sample S (Red) and FS-M (Black)

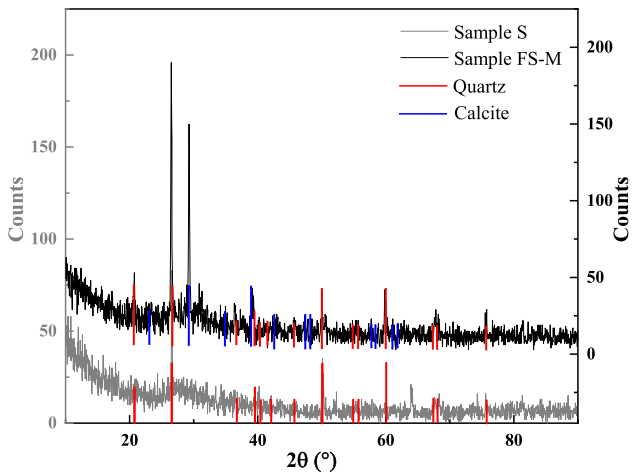

Fig. 13 1D XRD patterns of sample S (Gray) and sample FS-M (Black)

crystal plane of calcite. The peaks at 2θ = 16.97, 43.98, and 45.77° contributed to the crystal plane of whewellite. The crystal plane of weddellite contributed to the peaks at 2θ = 15.98, 21.81, 33.19 and 41.99°. The XRD peaks are sharp and intense, indicating a high crystallinity of the mineral precipitation by fungal mycelium in the FS-T sample.

5.3.2 The effects of hydrophobicity of fungi mycelium on shear force reduction

5.3.2.1 Hydrophobicity measurement with contact angle test The standard experimental measurement of hydrophobicity is the angle that a water droplet rests on the solid surface. The contact angle ranges from 180° down to 0°, with small contact angle indicating hydrophilic behavior and large contact angle indicating hydrophobic behavior. The contact angle of the ultrahydrophobic surface inspired by the lotus leaf can be as high as 177°; clean glass is highly hydrophilic, with contact angle close to 0° [23]. Five different mycelium film with dimensions of 1 × 1 cm were collected from sample FS-T, and the results of contact angle are summarized in Table 4. The equilibrium contact angle of each of the mycelium surfaces was found to be greater than 110° and the average contact angle is 116.42°. The contact angles at various locations show slight differences because the fungal mycelium surface is

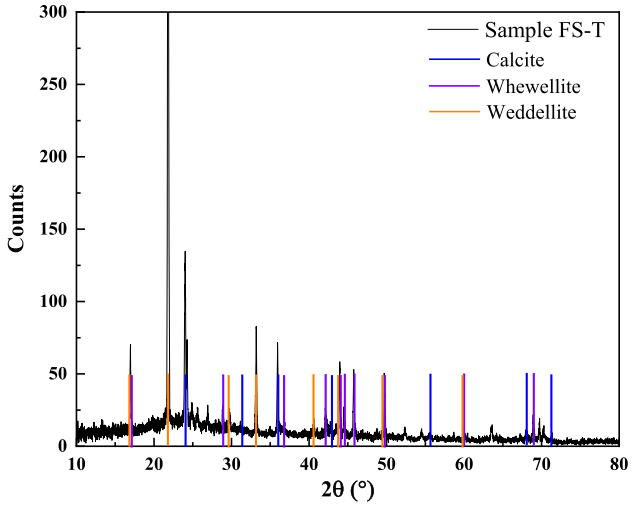

Fig. 14 2D XRD patterns of sample FS-T

Table 4 Contact angle (CA) measurement of fungal mycelium film

No	CA left (°)	CA right (°)	Averaged (°)
1	115.7	116.9	116.3
2	110.7	110.1	110.4
3	120.3	120.2	120.2
4	118.4	118.3	118.3
5	117.3	116.3	116.8
Mean	**116.48**	**116.36**	**116.42**

not smooth. Additionally, the micro-sized hyphae are not heterogenous. Both the hydrophobicity of fungal hyphae and the microscale surface features prevent the infiltration of water. The measurement results indicate the *P. ostreatus* mycelium feature hydrophobic properties.

5.3.2.2 Analyses of the effects of fungi hydrophobicity on interfacial shear force reduction The dynamics of water-soil interactions is influenced by the condition of the interface. The contact angles of various soil materials ranged from 14.8 to 20.8° [5]. For hydrophilic surfaces such as sand, the slip of Newtonian fluid flow is negligible at the interface, since the viscosity of fluid brings the water flow to rest at the boundary [42]. However, at hydrophobic surface such as fungi mediated soil, the water moves along a water-repellent wall and partially wetted surface, which causes a slip effect at the boundary. The hydrophobic surface due to low surface energy and topological micro-features improves the mobility of fluid and reduces shear stress at the interface [12, 29]. The difference between a common surface and a hydrophobic surface lies not only in the surface chemistry, but also in the microstructure of the surface. For instance, lotus leaves with micrometer-sized protrusions in hydrophobic wax, have well-known water-repellent properties [29]. The chemical hydrophobins on the surface of hyphae repel water; the microstructure of the hyphae network on the surface also increases the surface roughness. If the fluid slip occurs at the boundary, reduced shear force will be observed. The roughness on the hydrophobic surfaces contributing to hydrophobicity will result in larger shear force reduction [13].

To investigate the influence of hydrophobicity of fungi mediated soils on the soil–water boundary shear conditions on the interactions of flow and soil, Computational Fluid Dynamics (CFD) was utilized to simulate the flow field and interfacial shear stress in the SSTR experiment. The effects of hydrophobicity are simulated by applying proper boundary conditions, i.e., no-slip boundary and slip boundary. The simulation model was developed using the Rotating Machinery, Fluid Flow branch in CFD Module with the frozen-rotor study type to investigate the flow velocity distribution and shear stress at soil–water interface

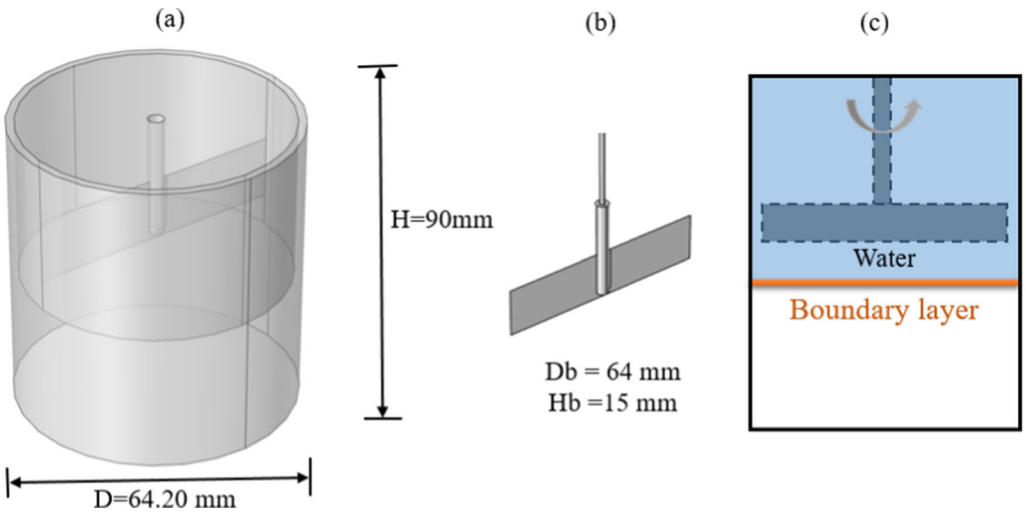

Fig. 15 SSRT numerical simulation model **a** Vessel **b** Bladed impeller **c** Schematic diagram of the Rotating Machine Model

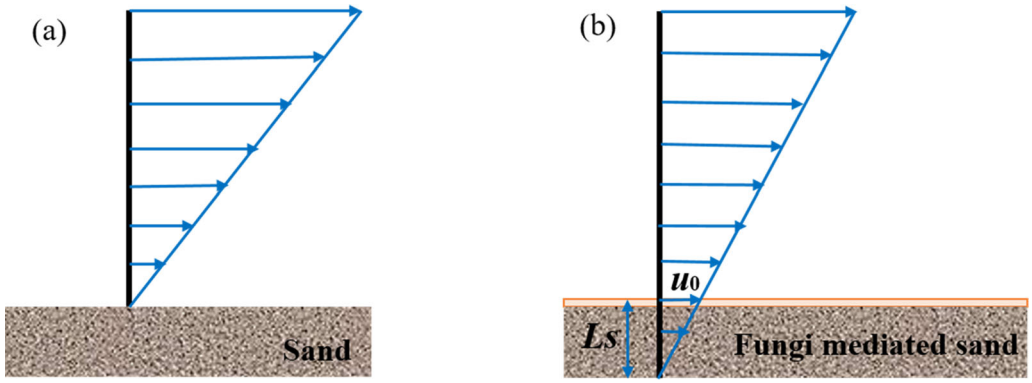

Fig. 16 Schematic diagram of streamline slip velocity at a water–solid interface **a** no-slip boundary of sand sample (S); **b** slip boundary of fungi mediated sand sample with slip length of *Ls* (FS-M)

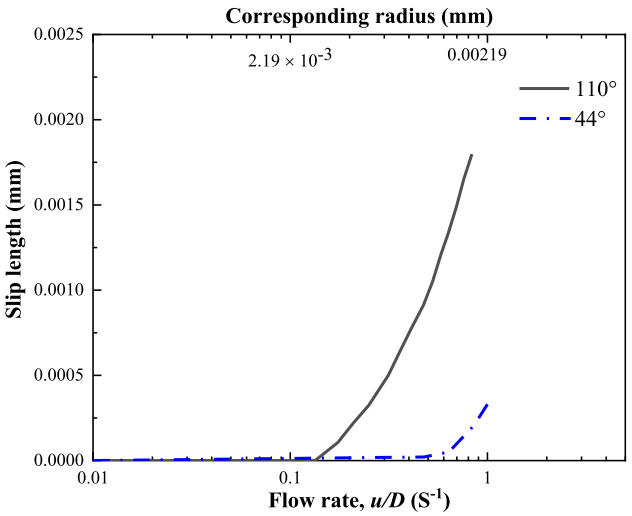

Fig. 17 The slip length increases with flow rate (bottom axis) and corresponding radius at 120 rpm (top axis) on the surface with a contact angle of 110 and 44°. *u* is flow velocity and *D* is boundary thickness. (Modified from [41])

under different boundary conditions. The numerical model was built with the geometry and boundary conditions of the SSRT experimental setup as shown in Fig. 15. The model consists of two physical components, i.e., a vessel and an impeller structure. The vessel used for SSRT consists of a vertical cylinder with a dish-shaped bottom. The rotation of the impeller drives the mixing of the fluid in the vessel to simulate the process of SSRT. The clearance is defined as the vertical distance between the lowest point on the cylindrical wall of the vessel and the mean vertical position of the impeller blades. No-slip boundary is applied on the bottom wall to simulate the water–solid interface in the control sample (S); slip boundary is applied on the fungi modified sand sample (FS-M). A no-slip boundary condition is set on the sidewall. Schematic of the streamline velocity at the water–solid interface under different boundary conditions is illustrated in Fig. 16.

Once the rotating speed is set, the pitched blade impeller expels the surrounding water axially as well as radially. The mixing process occurs in the fluid filed, forming a large zonal vortex. The vortex extends from the plane of the impeller to the bottom boundary and causes shear force on the boundary.

The torque on the impeller (M) is given by

$$M = \left|\hat{z} \cdot \int_A R \times T dA\right| \tag{2}$$

The power draw (P) is calculated by

$$P = \left|\omega \cdot \int_A R \times T dA\right| = |\omega| M \tag{3}$$

where $\hat{z}$ is the average value of z position, A is the surface area of the impeller, T is the total stress. ω is the angular-velocity vector.

The fluid equations for three-dimensional viscous water flow around the foundation can be solved by the Navier–Stokes equations (Eq. (4)). It assumes that the fluid is incompressible with the Mach number Ma > 0.3.

$$\rho(u \cdot \nabla)u + \rho \frac{\partial u}{\partial t} = \nabla \cdot \left[-pI + \mu(\nabla u + (\nabla u)^T\right] + F \tag{4}$$

$$\rho(u \cdot \nabla)u = 0 \tag{5}$$

where ρ is the fluid density, u is the flow velocity, μ is the dynamic viscosity, p is pressure, F is the applied force.

Different boundary conditions are applied at the water–solid interface. The no-slip boundary is applied to the boundary of sand sample (S).

$$u = 0 \tag{6}$$

The slip boundary is applied to the boundary of fungi-mediated sample (FS-M):

$$u \cdot \vec{n} = 0 \tag{7}$$

$$\left[-pI + \mu(\nabla u + (\nabla u)^T\right] \cdot \vec{n} = -\frac{\mu}{Ls} u \tag{8}$$

where Ls is the slip length.

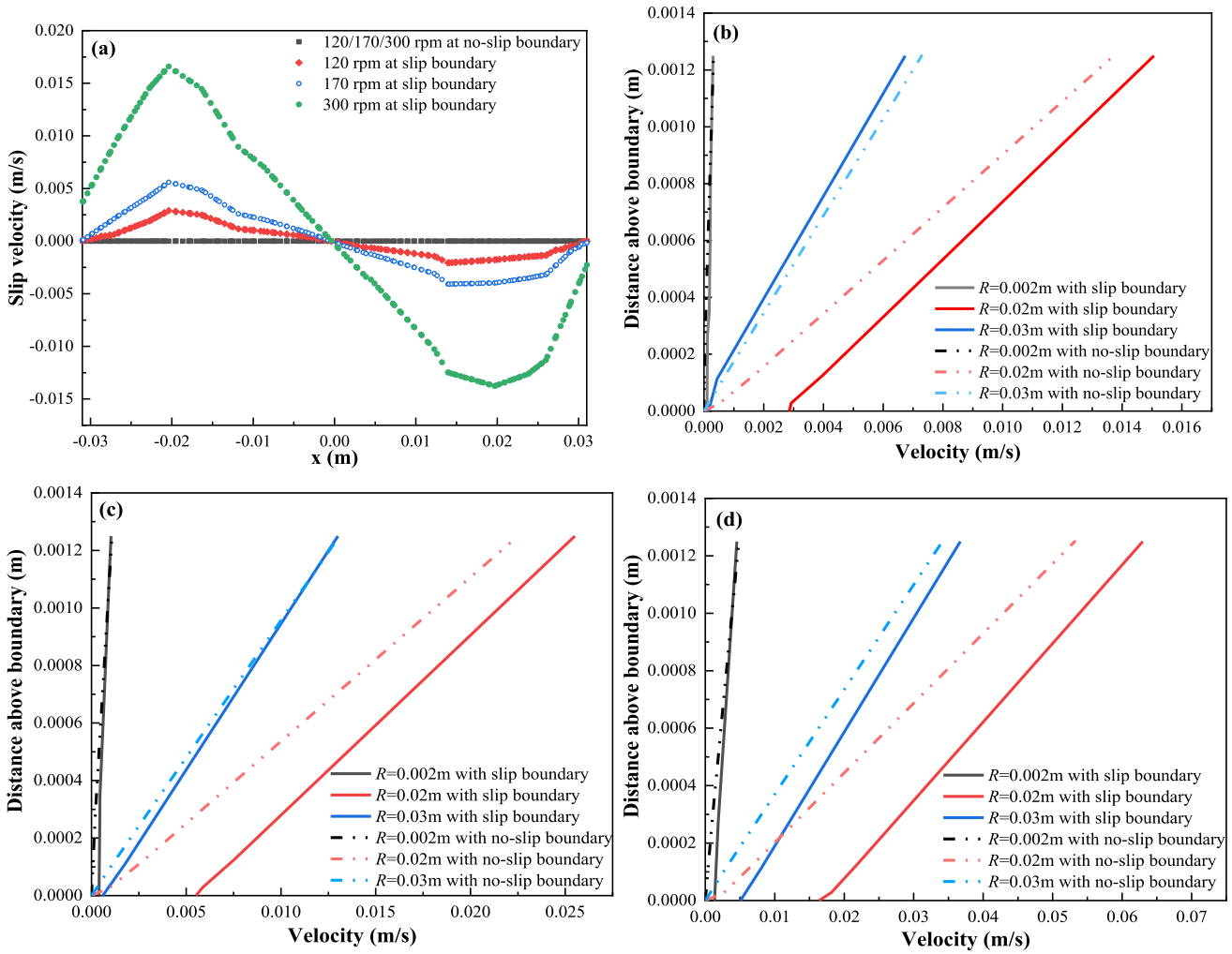

Fig. 18 The velocity profile **a** slip velocity at boundary surface along radius direction; velocity profile near boundary along vertical direction **b** at 120 rpm; **c** at 170 rpm; **d** at 300 rpm

5.4 The slip length Ls on the boundary surface of fungi-mediated soil sample

The slip length was applied on the hydrophobic surface of fungi-mediated samples at the microscale. Figure 17 shows the variation of slip length on the surfaces with contact angles of 110 and 44°, in which u is flow velocity and D is boundary layer thickness. The boundary thickness of the fungi-mediated soil sample is assumed the same as that of soil sample, or $D_{50}/2$, where D_{50} is the mean particle size (Wang, Yuan et al. 2021). The slip length is assumed to increase exponentially with the local flow rate and the maximum slip length is assumed to be the boundary thickness. Flow rate increases linearly along the radius in the SSRT. The maximum slip length ($D_{50}/2$) occurs at the radius of 0.16 mm at the blade rotation speed of 120 rpm. This range is much smaller than the diameter of the central shaft (2.92 mm) of the rotating blade and the diameter of soil samples (64.20 mm). In addition, Fig. 17 also shows that at same flow rate, the surface with a larger contact angle has a greater slip length (and therefore more shear stress reduction at the surface boundary). The CFD simulation was proceeded with slip length corresponding to 110°, which is the only data available from prior experiments that is closest to the contact angle of 116.42°. It is noted that the estimation of the effects of hydrophobicity on the shear stress reduction at the surface of fungi modified soils is to the conservative side. This further illustrates the potential benefits of fungi in mitigating soil erosion by reducing the erosive shear stress at the interface.

5.5 The impacts of boundary conditions on the interfacial shear stress

To investigate the impact of boundary conditions, the shear velocity on the surface with no-slip and slip boundary conditions under different rotating speeds (120, 170 and 300 rpm) is analyzed. The results are shown in Fig. 18a.

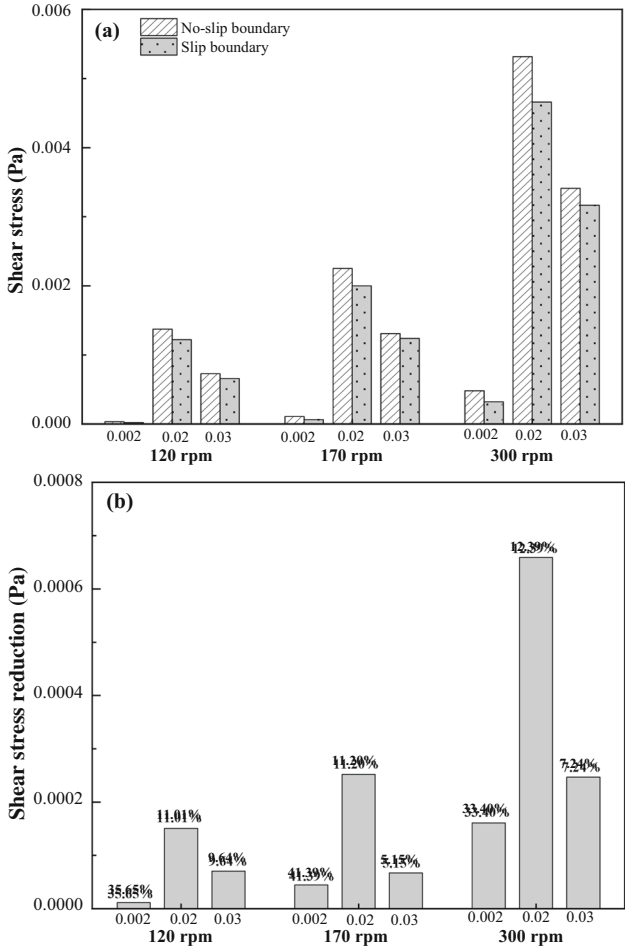

Fig. 19 **a** Effects of slip on boundary shear stress; **b** Shear stress reduction by slip boundary (absolute value and relative changes using non-slip as baseline)

Water flow on the surface with no-slip boundary condition, the velocity decreases to 0. However, the slip velocity exists on the surface under slip boundary condition; it increases first along the radius direction and decreases due to the influence of no-slip sidewalls. Larger slip velocity on the boundary is observed with the increase in rotating speed.

The velocity of water flow near the boundary decreases closer to the boundary. The velocity profiles at different locations under various rotating speeds are summarized in Fig. 18b–d. Compared with the control soil sample (Sample S) with no-slip boundary condition, the slope is smaller under slip boundary compared with non-slip boundary, which indicates smaller shear stress.

The shear stress near boundary is estimated by (Westenbroek 2006):

$$\tau = \rho u^* \tag{9}$$

τ is the bottom shear stress in dyn/cm^2 (1 dyn/cm^2 = 0.1 N/m^2 = 0.1 Pa), u^* is the shear velocity near the boundary.

The results of shear stresses at different blade rotation speeds under both no-slip boundary and slip boundary conditions are compared in Fig. 19. The slip condition reduces the shear stress at the water-soil boundary. The shear stress decreases more at a higher fluid speed. For example, the slip (due to hydrophobicity of fungi) reduces the boundary shear stress by 41.39% at the radius of 0.002 m under blade rotation speed of 170 rpm. The shear stresses are reduced by 33.40, 12.39 and 7.24% at a radius of 0.002, 0.02 and 0.03 m under rotating speed of 300 rpm. The reduced shear stress also helped to improve the erosion resistance of fungi-mediated soil samples.

6 Conclusions

This study investigated a novel strategy to improve soil erosion resistance with fibrous fungi. The experiment and analyses have identified two major mechanisms that led to higher erosion resistance by fungi mediated soils, i.e., (1) Improvement of soil by fungi fiber reinforcement and mineral precipitations and (2) Reduction of boundary shear stress on soil by flowing water due to hydrophobicity of fungi fibers. The specific conclusions from this study include:

(1) The particle size and embedment depth affect the behaviors of fungi germination and growth. From the observations, an optimal embedment depth was identified in this study.
(2) After inoculation, fungal mycelium germinated and covered the soil surface with a diameter of 64.20 mm in 15 days when inoculated on the top surface of soil and in 20 days when inoculated 5 mm under the soil surface.
(3) The fungi-mediated soil samples showed significantly improved erosion resistance compared with the control soil sample, both in terms of increasing the critical flow velocity and reducing the slope of erosion rate versus flow velocity curve. For example, inoculation of fungi at the surface of the sample improved the critical shear velocity from 0.2 to 0.4 m/s; inoculation of fungi in the middle of soil increased the shear velocity to be larger than 1.0 m/s.
(4) Measurement of the microstructure of fungi-mediated soil sample showed that the sand particles are reinforced by the entanglement of fungal hyphae and glued by the mineral precipitation produced by fungi. The precipitations were recognized calcite, calcium oxalate monohydrate and calcium oxalate dihydrate.

(5) The fungal mycelium demonstrated hydrophobic behaviors with a large contact angle of 116.42°.

Analyses with CFD simulation indicated that compared with natural soil, the slip produced by hydrophobicity of fungi reduced the shear stress at the water-soil interface by flowing water.

Overall, biochemical interactions between fungal and sand particles as well as the hydrophobicity of fungal mycelium improved the soil erosion resistance and therefore it implies a potential bio-based method for soil improvements. Fungal spores are highly tolerant and may live for several decades as spores. The inorganic biochemical precipitations generated by fungi remain stable after an extended period. These conditions all contribute to the long-term sustainability of fungi-mediated technique in soil.

Acknowledgements The authors would like to thank Jim Berilla for his assistance in SSRT setup. We also would like to thank Kuan Huang for his kind help with the FTIR test. The SEM/EDS as well as XRD data were obtained at the Characterization Facility of the Swagelok Center for Surface Analysis of Materials (SCSAM), Case Western Reserve University.

References

1. Akib S, Liana Mamat N, Basser H, Jahangirzadeh A (2014) Reducing local scouring at bridge piles using collars and geobags. Sci World J 2014:1–7
2. Attias N, Danai O, Abitbol T, Tarazi E, Ezov N, Pereman I, Grobman YJ (2020) Mycelium bio-composites in industrial design and architecture: Comparative review and experimental analysis. J Clean Prod 246:119037
3. Bao R (2017) Effect of Microbial Induced Carbonate Precipitation on Surface Erosion. University of Akron, UK
4. Bindschedler S, Cailleau G, Verrecchia E (2016) Role of fungi in the biomineralization of calcite. Minerals 6(2):41
5. Cawlfield GE (1962) The contact angle between water and soil materials, Montana State University-Bozeman College of Agriculture.
6. Chiew Y-M (1995) Mechanics of riprap failure at bridge piers. J Hydraul Eng 121(9):635–643
7. Chu J, Ivanov V, Naeimi M, Stabnikov V, Liu H-L (2014) Optimization of calcium-based bioclogging and biocementation of sand. Acta Geotech 9(2):277–285
8. Dash S, Kamruddin M, Ajikumar P, Tyagi A, Raj B (2000) Nanocrystalline and metastable phase formation in vacuum thermal decomposition of calcium carbonate. Thermochim Acta 363(1–2):129–135
9. El-Enshasy HA (2007) Filamentous fungal cultures–process characteristics, products, and applications. Bioprocessing Value-Added Pproduct Renew Res 1:225–261
10. Gow, N. A. and G. M. Gadd (2007). Growing fungus, Springer Science & Business Media.
11. Guo Y, Yang Y, Yu XB (2018) Influence of particle shape on the erodibility of non-cohesive soil: insights from coupled CFD–DEM simulations. Particuology 39:12–24
12. Haibao H, Peng D, Feng Z, Dong S, Yang W (2015) Effect of hydrophobicity on turbulent boundary layer under water. Exp Thermal Fluid Sci 60:148–156
13. Hao PF, Wong C, Yao ZH, Zhu KQ (2009) Laminar drag reduction in hydrophobic microchannels. Chem Eng Technol: Ind Chem-Plant Equip-Process Eng-Biotechnol 32(6):912–918
14. He J, Gray K, Norris A, Ewing AC, Jurgerson J, Shi X (2020) Use of biological additives in concrete pavements: a review of opportunities and challenges. J Trans Eng, Part B: Pav 146(3):04020036
15. Institute of Chemistry University of Tartu, E. "https://spectra.cs.ut.ee/paint/fillers/quartz/
16. Jin C, Yu R, Shui Z (2018) Fungi: a neglected candidate for the application of self-healing concrete. Front Built Environ 4:62
17. Jonkers HM, Thijssen A, Muyzer G, Copuroglu O, Schlangen E (2010) Application of bacteria as self-healing agent for the development of sustainable concrete. Ecol Eng 36(2):230–235
18. Lagasse PF (1999). 1998 Scanning review of european practice for bridge scour and stream instability countermeasures. NCHRP Res Results Digest(241)
19. Lagasse PF, Zevenbergen L, Spitz W, Arneson L (2012) Stream stability at highway structures, United States. Federal Highway Administration. Office of Bridge Technology
20. Lydan MA, Cotter DA (1995) The role of Ca2+ during spore germination in Dictyostelium: autoactivation is mediated by the mobilization of Ca2+ while amoebal emergence requires entry of external Ca2+. J Cell Sci 108(5):1921–1930
21. Mohamed YA, Abdel-Aal GM, Nasr-Allah TH, Shawky AA (2016) Experimental and theoretical investigations of scour at bridge abutment. J King Saud Univ Eng Sci 28(1):32–40
22. Money NP (2016) Spore production, discharge, and dispersal. Elsevier, The fungi, pp 67–97
23. Ou J, Perot B, Rothstein JP (2004) Laminar drag reduction in microchannels using ultrahydrophobic surfaces. Phys Fluids 16(12):4635–4643
24. Pinder R, Gilliland A, Dennis R (2008) Environmental impact of atmospheric NH3 emissions under present and future conditions in the eastern United States. Geophys Res Lett. https://doi.org/10.1029/2008GL033732
25. Presley, D and Tatarko J (2009). Principles of wind erosion and its control, Kansas State University Agricultural Experiment Station and Cooperative
26. Richardson, EV and Davis SR (2001). Evaluating scour at bridges, United States. Federal Highway Administration. Office of Bridge Technology
27. Rillig MC (2005) A connection between fungal hydrophobins and soil water repellency? Pedobiologia 49(5):395–399
28. Rodriguez-Blanco JD, Shaw S, Benning LG (2011) The kinetics and mechanisms of amorphous calcium carbonate (ACC) crystallization to calcite, via vaterite. Nanoscale 3(1):265–271
29. Rothstein JP (2010) Slip on superhydrophobic surfaces. Annu Rev Fluid Mech 42:89–109
30. Scholtmeijer K, Wessels J, Wösten H (2001) Fungal hydrophobins in medical and technical applications. Appl Microbiol Biotechnol 56(1):1–8
31. Shirole A, Holt R (1991) Planning for a comprehensive bridge safety assurance program. Transp Res Rec 1290:39–50
32. Stocks-Fischer S, Galinat JK, Bang SS (1999) Microbiological precipitation of CaCO3. Soil Biol Biochem 31(11):1563–1571
33. Wang C, Yu X, Liang F (2017) A review of bridge scour: mechanism, estimation, monitoring and countermeasures. Nat Hazards 87(3):1881–1906
34. Wang C, Yuan Y, Liang F, Yu XB (2021) Investigating the effect of grain composition on the erosion around deepwater foundations with a new simplified scour resistance test. Transp Geotech 28:100527

35. Wang X, Tao J, Bao R, Tran T, Tucker-Kulesza S (2018) Surficial soil stabilization against water-induced erosion using polymer-modified microbially induced carbonate precipitation. J Mater Civ Eng 30(10):04018267
36. Wang X, Ye A, Ji B (2019) Fragility-based sensitivity analysis on the seismic performance of pile-group-supported bridges in liquefiable ground undergoing scour potentials. Eng Struct 198:109427
37. Zhang F, Dai G, Gong W (2021) Analytical method for laterally loaded piles in soft clay considering the influence of soil outside the scour hole on the effective overburden pressure. Acta Geotechn 16:1–12
38. Zhang X, Fan X, Han C, Li Y, Price E, Wnek G, Liao Y-TT, Yu XB (2021) Novel strategies to grow natural fibers with improved thermal stability and fire resistance. J Clean Prod 320:128729
39. Zhang X, Fan X, Li M, Samia A, Yu XB (2021) Study on the behaviors of fungi-concrete surface interactions and theoretical assessment of its potentials for durable concrete with fungal-mediated self-healing. J Clean Prod 292:125870
40. Zhao W, Sharma N, Jones F, Raiteri P, Gale JD, Demichelis R (2016) Anhydrous calcium oxalate polymorphism: a combined computational and synchrotron X-ray diffraction study. Cryst Growth Des 16(10):5954–5965
41. Zhu Y, Granick S (2001) Rate-dependent slip of Newtonian liquid at smooth surfaces. Phys Rev Lett 87(9):096105
42. Zhu Y, Granick S (2002) Limits of the hydrodynamic no-slip boundary condition. Phys Rev Lett 88(10):106102